NASA SP-315

APOLLO 16

Preliminary Science Report

PREPARED BY

NASA MANNED SPACECRAFT CENTER

Scientific and Technical Information Office 1972

NATIONAL AERONAUTICS AND SPACE ADMINISTRATION

Washington, D.C.

11. Lunar Surface Magnetometer Experiment

P. Dyal,[a†] C. W. Parkin,[a] D. S. Colburn,[a] and G. Schubert[b]

INTRODUCTION

The Apollo 16 lunar surface magnetometer (LSM), which was activated at 20:22 G.m.t. on April 21, 1972, completed the network installation of magnetic observatories on the lunar surface and initiated simultaneous measurements of the global response of the Moon to large-scale solar and terrestrial magnetic fields. Analysis of long-term simultaneous measurements by widely separated surface magnetometers will greatly enhance the previous single-instrument studies of lunar internal electrical conductivity and temperature, internal magnetic permeability, and surface remanent magnetic fields.

A continuous electrical conductivity profile of the lunar interior has been calculated by analysis of the decay of eddy-current magnetic fields induced in the Moon by solar field step transients. The conductivity is in turn related to internal temperature, which is calculated for assumed lunar material compositions.

The relative magnetic permeability of the outer layers of the Moon has been calculated from measurements obtained when the Moon was immersed in the geomagnetic tail field. The permeability is related to the amount of permeable material, such as iron, that exists in the outer layers of the Moon.

Fossil remanent magnetic fields have been measured at nine locations on the lunar surface, including the Apollo 16 LSM site in the Descartes highlands area. Remanent fields provide a record of the magnetic field environment that existed at the Moon 3 to 4 billion years ago at the time the crustal material cooled below the Curie temperature. This fossil record indicates the possible existence of an ancient lunar dynamo or a solar or terrestrial field much stronger than exists at present.

THEORY

The external driving magnetic field in the lunar environment can vary considerably with the lunar orbital position. (See fig. 11-1.) Average magnetic field conditions vary from relatively steady fields of magnitude of approximately 9 γ (1 γ = 1 nT) in the geomagnetic tail to mildly turbulent fields averaging ~5 γ in the free-streaming solar plasma region to turbulent fields averaging 8 γ in the magnetosheath. Average solar wind velocity is approximately 400 km/sec in a direction approximately along the Sun-to-Earth line.

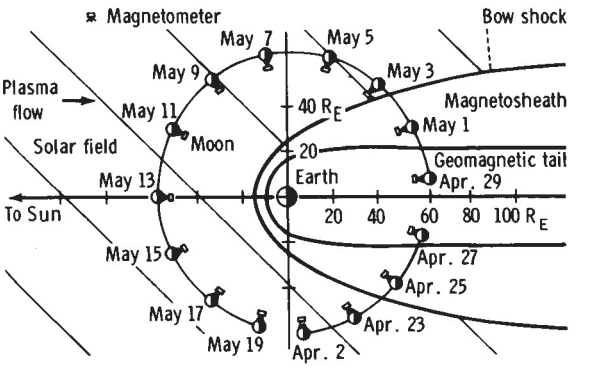

FIGURE 11-1.–Lunar orbit projection onto the solar ecliptic plane, showing the Apollo 16 LSM during the first postdeployment lunation. During a complete revolution around the Earth, the magnetometer passes through the Earth bow shock, the magnetosheath, the geomagnetic tail, and the interplanetary region dominated by solar plasma fields.

Various induced lunar and plasma-interaction fields also exist at the lunar surface; for reference, the sum of these fields is written

$$\mathbf{B}_A = \mathbf{B}_E + \mathbf{B}_S + \mathbf{B}_\mu + \mathbf{B}_P + \mathbf{B}_T + \mathbf{B}_D + \mathbf{B}_F \quad (11\text{-}1)$$

Here $\mathbf{B}_A$ is the total magnetic field measured on the surface by an Apollo LSM; $\mathbf{B}_E$ is the total external (solar or terrestrial) driving magnetic field measured by the Explorer 35 magnetometer and the Apollo 15

[a]NASA Ames Research Center.
[b]University of California at Los Angeles.
[†]Principal Investigator.

and 16 subsatellite lunar orbiting magnetometers while outside the antisolar lunar cavity; $\mathbf{B}_S$ is the steady remanent field at the surface site; $\mathbf{B}_\mu$ is the global magnetization field induced in permeable lunar material; $\mathbf{B}_P$ is the poloidal field caused by eddy currents induced in the lunar interior by changing external fields; $\mathbf{B}_T$ is the toroidal field corresponding to unipolar electrical currents driven through the Moon by the $\mathbf{V} \times \mathbf{B}_E$ electric fields (where $\mathbf{V}$ is the velocity of the Moon with respect to the solar wind); $\mathbf{B}_D$ is the field associated with the diamagnetic lunar cavity; and $\mathbf{B}_F$ is the total field associated with the hydromagnetic solar wind flow past the Moon. The relative importance of these different fields varies with orbital position; therefore, different magnetic fields and lunar properties can be investigated during selected times of each lunation.

Electrical Conductivity and Temperature

When the Moon is immersed in a free-streaming solar wind and the magnetometer is located on the dark (antisolar) side of the Moon and isolated from solar plasma flow, then $\mathbf{B}_F \rightarrow 0$ and $\mathbf{B}_\mu$ and $\mathbf{B}_T$ can be neglected (ref. 11-1). Equation (11-1) therefore reduces to

$$\mathbf{B}_A = \mathbf{B}_P + \mathbf{B}_E + \mathbf{B}_S \qquad (11\text{-}2)$$

where cavity effects $\mathbf{B}_D$ are neglected to a first approximation for selected measurements made near lunar midnight (ref. 11-2). After $\mathbf{B}_S$ has been calculated from geomagnetic tail data, only the poloidal field $\mathbf{B}_P$ is unknown. Equation (11-2) can then be solved for certain assumed lunar models, and curve fits of data to the solution determine the model-dependent conductivity profile $\sigma(R)$. Furthermore, electrical conductivity is related to temperature, and the lunar interior temperature can be calculated for assumed lunar material compositions.

It is useful to consider the idealized case in which the Moon is represented by a uniformly conducting sphere in a vacuum. This case is solved analytically by Smythe (ref. 11-3). Assume that initially there is no magnetic field but, at a time $t = 0$, an external magnetic field $\Delta\mathbf{B}_E$, which is uniform far from the sphere, is switched on. At this time, a surface current is induced on the sphere, which excludes the applied field completely from the interior (fig. 11-2). The current then diffuses through the sphere and eventually decays to zero strength. Correspondingly, the external field (which was originally excluded) diffuses into the sphere so that, finally, a uniform field occupies all space. If the conductivity of the sphere is large, the eddy currents will be sustained for a long time, and the external field will only slowly diffuse to the interior. At the surface, the tangential component of the field is initially greater than the corresponding external field component, and the radial surface component is initially zero (fig. 11-3). Both components asymptotically approach the values of external field components as the induced currents decay.

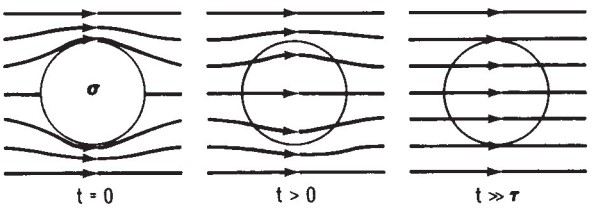

FIGURE 11-2.–Transient magnetic response of a conducting sphere in a magnetic field. At the time of the step transient $t = 0$, eddy currents are generated that exclude field lines to the outer edge of the sphere. At later times, the eddy currents diffuse inward, permitting the field lines to permeate the entire sphere at a time much greater than the time response τ of the conductor.

The response of the Moon, as measured by the Apollo 12 magnetometer on the dark side, is qualitatively similar to the curves shown in figure 11-3. (The response deviates from these curves insofar as the electrical conductivity of the Moon is not homogeneous.) To determine the conductivity profile from the shape of the transient response curves, it is assumed that the dark-side response is that of a sphere in a vacuum. This assumption is justified by the low plasma density on the dark-side surface reported by Snyder et al. (ref. 11-4). Furthermore, it has been found that the lunar response is not a function of position if the magnetometer is more than 400 km inside the optical shadow. Therefore, the effect of currents at the boundary of the lunar cavity (and on the front surface of the Moon) on the shape of the response curves is neglected. It has been shown that the currents in the Moon driven by the solar wind $\mathbf{V} \times \mathbf{B}_E$ field can be neglected (ref. 11-1). The driving field is taken to be spatially uniform, which requires that its scale be much greater than the diameter of the Moon and that the discontinuity be swept past

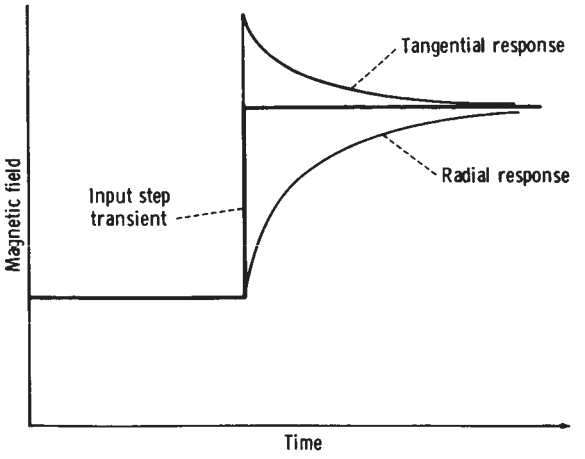

FIGURE 11-3.–Theoretical solutions for the lunar-night vacuum poloidal magnetic field response of a homogeneous conducting sphere to a step function transient in the driving solar wind magnetic field. For a step function change ΔB_E in the external driving field (measured by Explorer 35), the total magnetic field at the surface of the Moon B_A (measured by the Apollo 12, 15, and 16 magnetometers) will be damped in the radial B_{Ax} component and will overshoot in the tangential (B_{Ay} and B_{Az}) components.

the Moon in a time that is short compared with the lunar response time. Both of these conditions are generally fulfilled. Based on these assumptions, it is possible to model the dark-side transient response by that of an inhomogeneous conducting sphere in a vacuum. The solution of the vector diffusion equation for the transient magnetic response of a sphere with radial conductivity distribution $\sigma(R)$ to an arbitrary input $b(t)$ is described in detail in reference 11-5. By assuming the material composition of the lunar interior and using a known conductivity-temperature relationship of that material, an internal radial temperature distribution can be calculated.

Magnetic Permeability and Steady Remanent Fields

When the Moon is passing through a quiet region of the geomagnetic tail, solar wind interaction fields ($\mathbf{B}_T$, $\mathbf{B}_D$, and $\mathbf{B}_F$) and the induced poloidal lunar field $\mathbf{B}_P$ are negligible, and equation (11-1) for the total field at the lunar surface reduces to

$$\mathbf{B}_A = \mathbf{B}_E + \mathbf{B}_\mu + \mathbf{B}_S \qquad (11\text{-}3)$$

The magnetic moment m_μ of the field $\mathbf{B}_\mu$ is proportional to $\mathbf{B}_E$; that is, $m_\mu = K\mathbf{B}_E$. (The proportionality constant K in turn depends on the permeability and the dimensions of the permeable region of the Moon.) The magnetization of the lunar sphere by the Earth magnetic field is shown schematically in figure 11-4.

For the case of a homogeneous permeable lunar shell, equation (11-3) can be written in the following component form (ref. 11-6).

$$B_{Ax} = (1 + 2F)B_{Ex} + B_{Sx} \qquad (11\text{-}4)$$

$$B_{Ay,z} = (1 - F)B_{Ey,z} + B_{Sy,z} \qquad (11\text{-}5)$$

where

$$F = \frac{(2k_m + 1)(k_m - 1)\left[1 - \left(\frac{R}{R_m}\right)^3\right]}{(2k_m + 1)(k_m + 2) - 2\left(\frac{R}{R_m}\right)^3(k_m - 1)^2} \qquad (11\text{-}6)$$

Here k_m is the relative permeability μ/μ_O, R_m is the lunar radius, and R is the radius of the boundary that encloses lunar material with a temperature above the Curie point. The coordinate system origin is at the magnetometer location on the lunar surface with x directed radially outward from the surface, y eastward, and z northward.

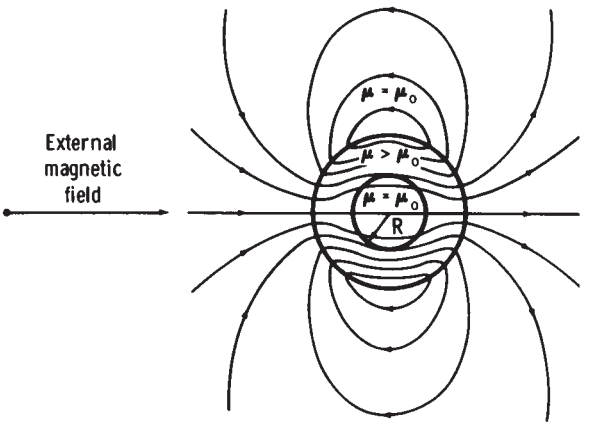

Note: For bulk permeability (the case R = 0), $\mu/\mu_0 = 1.01$.

FIGURE 11-4.–Induced magnetization field $\mathbf{B}_\mu$. A global permeable shell of material of permeability $\mu > \mu_O$ placed in the uniform geomagnetic tail tends to concentrate the field lines inside the shell.

Solar Wind Interaction

When the Moon is immersed in free-streaming solar wind and the magnetometer is on the lunar sunlit side, $\mathbf{B}_D \rightarrow 0$ outside the cavity, and the global fields $\mathbf{B}_\mu$ and $\mathbf{B}_T$ can be neglected (ref. 11-2). During times of high solar wind particle density, the interaction term $\mathbf{B}_F$ cannot be neglected; therefore, for daytime magnetometer data, equation (11-1) becomes

$$\mathbf{B}_A = \mathbf{B}_E + \mathbf{B}_S + \mathbf{B}_P + \mathbf{B}_F \qquad (11\text{-}7)$$

At low frequencies ($<3 \times 10^{-4}$ Hz), $\mathbf{B}_P \rightarrow 0$, and the interaction field $\mathbf{B}_F$ can be investigated in terms of measured fields by reference to equation (11-2) in a form rewritten and defined for the low-frequency case as

$$\Delta\mathbf{B} = \mathbf{B}_A - \left(\mathbf{B}_E + \mathbf{B}_S\right) = \mathbf{B}_F \qquad (11\text{-}8)$$

It is found that, during times of high solar wind density, the remanent lunar surface magnetic field is compressed by the solar wind, as determined from simultaneous measurements of the LSM and the solar wind spectrometer (ref. 11-7). This interaction between the solar wind and the local remanent magnetic field is shown schematically in figure 11-5.

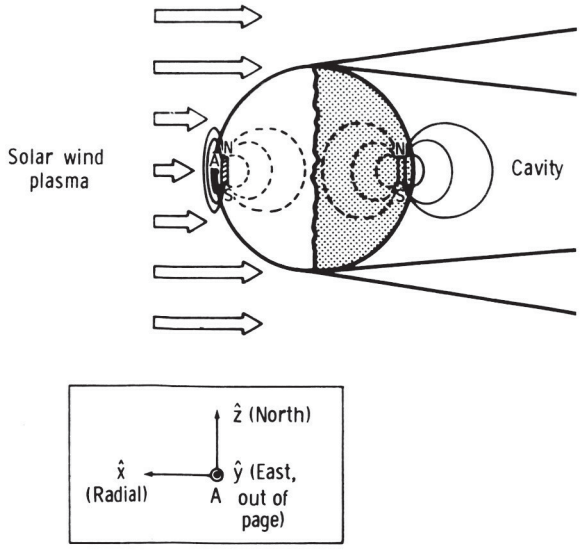

FIGURE 11-5.–Compression of a local remanent magnetic field by a high-density solar wind plasma. The remanent field is unperturbed during lunar night (antisolar side), while on the sunlit side the horizontal components are compressed. The inset shows the coordinate system used.

EXPERIMENTAL TECHNIQUE

For the experimental technique used to measure the magnetic field, the astronauts were required to deploy an LSM that would continuously measure and transmit information by radio to Earth for a period of at least 1 yr. A photograph of the LSM fully deployed and alined at the Descartes landing site is shown in figure 11-6, and the Apollo 16 LSM characteristics are given in table 11-I. (A detailed description of this instrument is provided in reference 11-8.)

FIGURE 11-6.–The Apollo 16 LSM deployed on the Moon in the lunar highlands. Sensors are at the top ends of the booms and approximately 75 cm above the lunar surface.

Fluxgate Sensor

The three orthogonal vector components of the magnetic field are measured by three fluxgate sensors designed and fabricated by the Naval Ordnance Laboratory (refs. 11-9 and 11-10). Each sensor, shown schematically in figure 11-7, consists of a toroidal Permalloy core that is driven to saturation by a sinusoidal current having a frequency of 6000 Hz. The sense winding detects the superposition of the drive-winding magnetic field and the total lunar surface field; as a result, a second harmonic of the driving frequency is generated in the sense winding with a magnitude that is proportional to the strength of the surface field. The phase of the second harmonic signal with respect to the drive signal indicates the direction of the surface field with respect to the sensor axis. This output signal is amplified and synchronously demodulated to drive a

voltage to the analog-to-digital converter and then through the central-station radio to Earth.

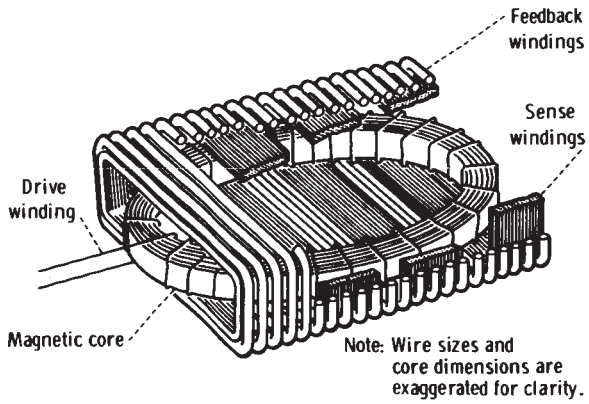

FIGURE 11-7.–Simplified view of the ring core magnetometer sensor developed jointly by the Naval Ordnance Laboratory and NASA Ames Research Center.

TABLE 11-I.–Apollo 16 Magnetometer Characteristics

Parameter	*Value*
Range, γ	0 to ± 200 0 to ± 100 0 to ± 50
Resolution, γ	±0.1
Frequency response	dc to 3 Hz
Angular response	Proportional to cosine of angle between magnetic field vector and sensor axis
Sensor geometry	3 orthogonal sensors at the ends of 100-cm booms; orientation determination to within 1° in lunar coordinates
No. of commands	
Ground	10
Spacecraft	1
Analog zero determination	180° flip of sensor
Internal calibration, percent of full scale	0, ±25, ±50, and ±75
Field bias offset capability, percent of full scale	0, ±25, ±50, and ±75
Modes of operation	Orthogonal field measurements, gradient measurement, internal calibration
Average power, W	
Day	3.5
Night	9.4
Weight, kg	8.9
Size, cm	25 by 28 by 63
Operating temperature, °K	223 to 358

Electronics

The electronic components for the LSM are located in the thermally insulated box. The operation of the electronics is illustrated in figure 11-8. Long-term stability is attained by extensive use of digital circuitry, by internal calibration of the analog portion of the instrument every 18 hr, and by mechanical rotation of each sensor through 180° to determine the sensor zero offset. The analog output of the sensor electronics is internally processed by a low-pass digital filter and a telemetry encoder; the output is transmitted to Earth via the central-station S-band transmitter. A typical internal flip-calibration sequence of the Apollo 16 instrument is shown in figure 11-9.

The LSM has two data samplers: the analog-to-digital converter (26.5 samples/sec) and the central-station telemetry encoder (3.3 samples/sec). The prealias filter following the sensor electronics has attenuations of 3 dB at 1.7 Hz, 64 dB at 26.5 Hz, and 58 dB at the Nyquist frequency (13.2 Hz), with an attenuation rate of 22 dB/octave. The four-pole Bessel digital filter limits the alias error to less than 0.05 percent and has less than 1 percent overshoot for a step function response. This filter has an attenuation of 3 dB at 0.3 Hz and 48 dB at the telemetry-sampling Nyquist frequency (1.6 Hz). The phase response is linear with frequency. The response of the entire LSM measurement system to a step function input is shown in figure 11-10. The digital filter can be bypassed by ground command in order to pass higher frequency information.

Mechanical and Thermal Subsystems

In the exterior mechanical and thermal configuration of the Apollo 16 LSM, the three fluxgate sensors are located at the ends of three 100-cm-long orthogonal booms that separate the sensors from each other by 150 cm and position them 75 cm above the lunar surface (fig. 11-6). Orientation measurements with respect to lunar coordinates are made with two devices. A shadowgraph and bubble level are used by the astronaut to aline the LSM and to measure azimuthal orientation with respect to the Moon-to-Sun line to an accuracy of 0.5°. Gravity-level sensors measure instrument tilt angles to an accuracy of 0.2° every 4.8 sec.

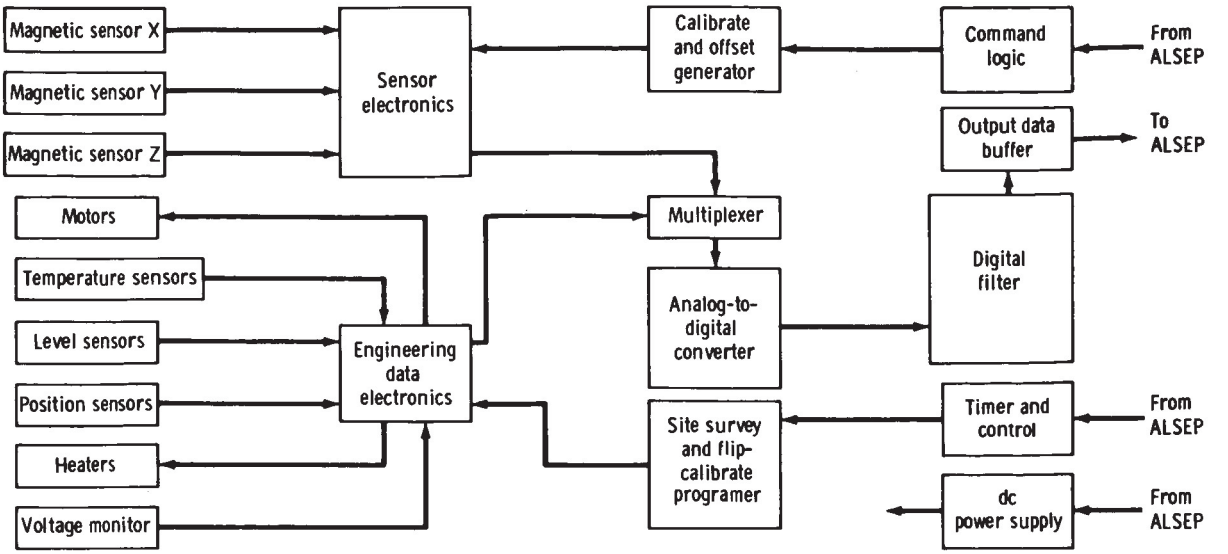

FIGURE 11-8.–Functional block diagram for the LSM electronics.

In addition to the instrument normal mode of operation in which three vector field components are measured, the LSM has a gradiometer mode in which commands are sent to operate three motors, which rotate the sensors such that all simultaneously aline parallel, first to one of the three boom axes, then to each of the other two boom axes in turn. This rotating alinement permits the vector gradient to be calculated in the plane of the sensors and also permits an independent measurement of the magnetic field vector at each sensor position.

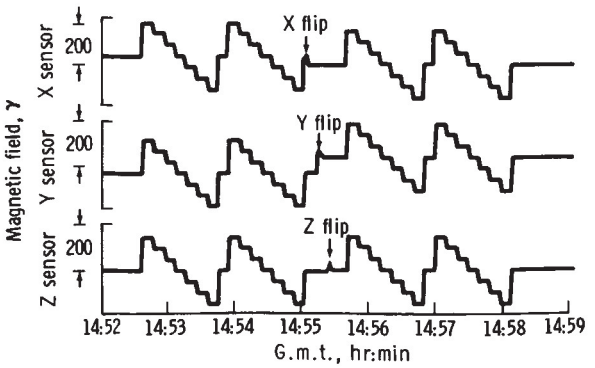

FIGURE 11-9.–Magnetometer data obtained during an internal flip-calibration sequence on April 26, 1972. This sequence is periodically repeated on command and involves internally generated biases in steps of 75, 50, 25, 0, -25, -50, and -75 percent of full scale.

The thermal subsystem is designed to allow the LSM to operate over the complete lunar day-night cycle. Thermal control is accomplished by a combination of insulation, control surfaces, and heaters that operate collectively to keep the electronics between 267° K and 319° K. A plot of the temperature of the X sensor and the electronics for the first postdeployment lunation is shown in figure 11-11.

Data Flow and Mission Operation

The LSM experiment is controlled from the NASA Manned Spacecraft Center (MSC) by commands transmitted to the Apollo lunar surface experiments package (ALSEP) from remote tracking stations. The data are recorded on magnetic tape at the remote sites and are also sent directly to MSC for real-time analysis to establish the proper range, offset, frequency response, thermal control, and operating mode. The one-time gradiometer-mode sequence of commands was successfully executed on April 28.

Explorer 35 Magnetometer

The ambient steady-state and time-dependent magnetic fields in the lunar environment are measured by the Explorer 35 satellite magnetometer. The satellite has an orbital period of 11.5 hr, an apolune of 9390 km, and a perilune of 2570 km (fig. 11-12). The Explorer 35 magnetometer measures three magnetic field vector components every 6.14 sec and has

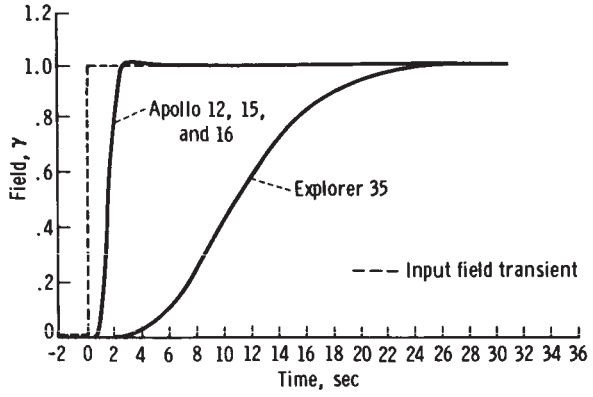

FIGURE 11-10.–Laboratory measurements comparing instrument transient responses of the Apollo 12, 15, and 16 and Explorer 35 magnetometers to a 1.0-γ magnetic step input.

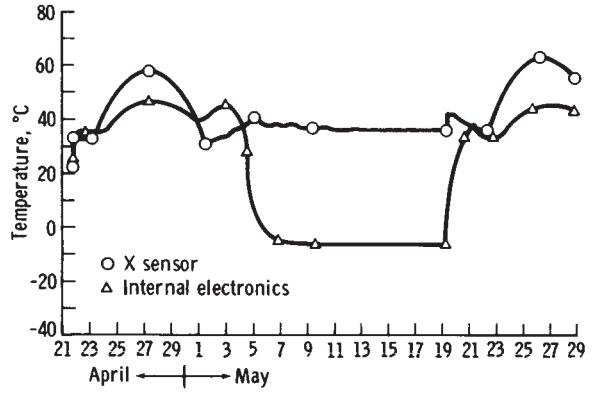

FIGURE 11-11.–Temperature inside one of the fluxgate sensors and inside the electronics box during the first postdeployment lunation of Apollo 16.

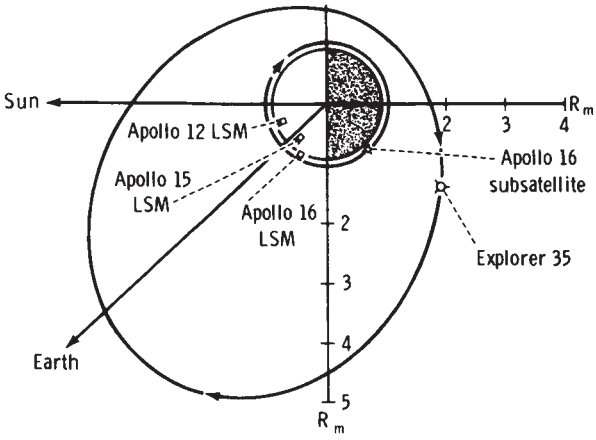

FIGURE 11-12.–The Explorer 35 orbit around the Moon, projected onto the solar ecliptic plane. The period of revolution is 11.5 hr. The Apollo 12, 15, and 16 surface instrument positions and Apollo 16 subsatellite trajectory are shown.

an alias filter with 18 dB attenuation at the Nyquist frequency (0.08 Hz) of the spacecraft data-sampling system. This instrument has a phase shift linear with frequency, and its step-function response is slower than that of the Apollo 12 instrument (fig. 11-10). Further information about the Explorer 35 magnetometer is contained in reference 11-8. Figure 11-12 also shows the orbit of the Apollo 16 particles and fields subsatellite that carries a magnetometer. Additional information on the subsatellite magnetometer is available in section 23 of this report.

RESULTS AND DISCUSSION

Internal Electrical Conductivity Calculations

Electrical conductivity and temperature profiles of the interior of the Moon can be calculated from magnetic transient response measurements made by lunar surface magnetometers on the dark (antisolar) side of the Moon. (A detailed discussion of this calculation is presented in reference 11-5.) The transient-response analytical method is described in the following paragraphs.

A discontinuity in the interplanetary magnetic field that is swept by the Moon induces eddy currents within the Moon. These currents induce a field that tends to oppose the external field, retarding its penetration of the Moon. The currents diffuse and decay in a manner governed by the lunar electrical conductivity distribution. The transient behavior of the induced magnetic field (recorded at the surface by the Apollo lunar surface magnetometers) is related to the conductivity function through the diffusion equation for the induced fields. Hence, the experimental method consists of scanning time-series data from the lunar orbiting Explorer 35 magnetometer (which monitors the solar wind field undisturbed by eddy currents within the Moon) to find interplanetary field discontinuities in the time record of the data from Explorer 35 that have smooth fields before and after the discontinuity. Then the corresponding induced field response recorded at the lunar surface is examined. Finally, a conductivity distribution is sought, which yields this response as a solution of the magnetic field diffusion equation.

From simultaneous radial-component data of a single LSM and the lunar orbiting Explorer 35 magnetometer, a radial electrical conductivity profile can be calculated from the decay characteristics of

the lunar eddy-current field $\mathbf{B}_P$ by a step transient in the solar field. Figure 11-13 shows normalized data from the Apollo 12 and Explorer 35 magnetometers, giving the lunar eddy-current field decay function obtained from radial field components for 11 clean step transient events. In all cases, the Apollo 12 data have been normalized by dividing by the Explorer 35 step magnitude to give the response to an effective unit step driving field.

All these events occurred when the magnetometer was more than 900 km inside the optical shadow; therefore, plasma effects are assumed to be absent, and classical theory of the response of a conducting sphere in a vacuum can be used. The error bars are standard deviations of the measurements.

The theoretical response curves (ref. 11-5) corresponding to a large number of lunar conductivity profiles were compared with the data shown in figure 11-13. It is found that a range of monotonic conductivity profiles, defining the shaded region in figure 11-14, provides fits to the data curve that fall within the error bars. The early response ($t < 20$ sec) is dominated by the finite rise time of the driving function; hence, detailed information on the conductivity at shallow depths is limited. However, it can be calculated that, for the first 90 km into the lunar surface, the average dc electrical conductivity must be very low: less than 10^{-9} mho/m (ref. 11-1).

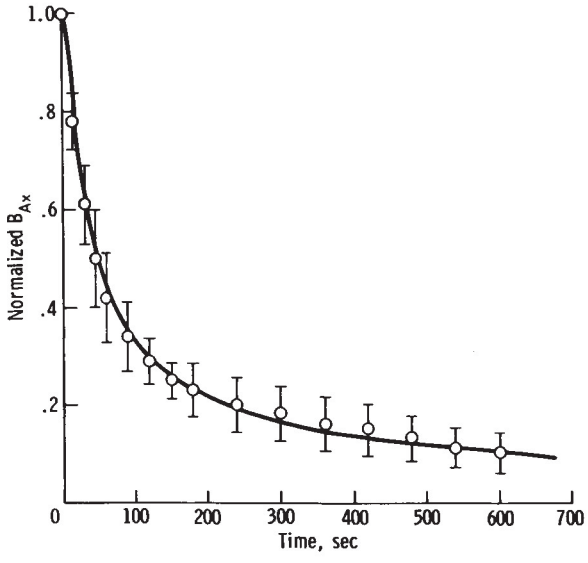

FIGURE 11-13.–Normalized transient response data, showing decay characteristics of the radial component of the total surface field B_{Ax}, after arrival of a step transient that changes the external magnetic field radial component by an amount ΔB_{Ex}, here normalized to a value of 1.

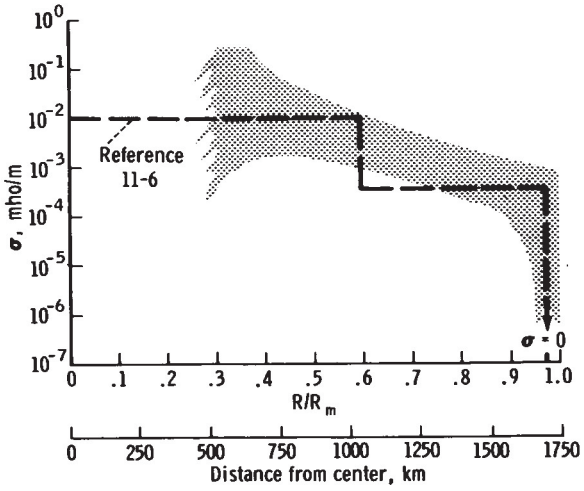

FIGURE 11-14.–Range of electrical conductivity profiles that give radial response time-dependent curves $f(t)$ that fall within the error bars of figure 11-13. A step function input magnetic field, modified by an initial ramp input of 15-sec rise time, is used in the analysis. The information at shallow depths is limited by the uncertainty in the rise time of the interplanetary magnetic field. At large depths, the information is limited by the sensitivity of the LSM.

For intermediate depths, however, the data allow only a rather restricted range of conductivities if the conductivity function is monotonic; hence, the shape of the data curve puts fairly restrictive limits on the conductivity in this region. From depths of approximately 90 km to approximately 1000 km (the region comprising the bulk of the volume of the Moon), the conductivity is seen to rise from approximately $10^{-3.5}$ to 10^{-2} mho/m. For the core region 1000 km into the Moon, there is an inherent limitation on the conductivity information to be gained from the data. (Indeed, a perfectly conducting lunar core with a radius of about 300 km would be undetectable even with large magnitude (approximately 40 γ) inputs.) Conductivities greater than $10^{-1.5}$ mho/m for depths >1000 km are compatible with the transient data.

Internal Temperature Calculations

By assuming the material composition of the lunar interior and by using a known conductivity-temperature relationship of that material, an internal temperature distribution of the Moon can be calculated from its conductivity profile. Figure 11-15 was

obtained by using the expressions for the electrical conductivity as a function of temperature given by England et al. (ref. 11-11) for olivine and peridotite, together with the results shown in figure 11-14 for the lunar conductivity. For the example of a peridotite Moon, a temperature profile that rises sharply to 850° to 1050° K at $R/R_m \sim 0.95$ and then rises gradually to 1200° to 1500° K at $R/R_m = 0.4$ is suggested by the data. At depths greater than $R/R_m = 0.4$, the temperature could be higher than 1500° K.

For description purposes, the Moon can be divided into three conductivity regions, as noted by the lunar three-layer conductivity profile superimposed on figure 11-14. Shown in figure 11-16 are the corresponding three regions, which include a thin outer crust of low conductivity and temperature; an inner shell, comprising the bulk of the lunar volume and of average temperature 900° to 1100° K; and a "core" region of temperature 1100° to 1500° K down to $R/R_m = 0.4$, with possible higher temperatures for $R/R_m < 0.4$.

Internal Magnetic Permeability Calculations

The magnetic permeability of the outer shell of the Moon (where temperatures are below the Curie point) can also be calculated from simultaneous Explorer 35 magnetometer and Apollo LSM data during times when the Moon is magnetized by the steady geomagnetic tail field. Explorer 35 provides a measurement of the steady magnetizing field $\mathbf{B}_E$, whereas the Apollo LSM measures the total field $\mathbf{B}_A = \mathbf{B}_E + \mathbf{B}$ (where the latter term is the magnetization field induced in the Moon). Because $\mathbf{B}_E$ is generally of magnitude less than ~15 γ in the geomagnetic tail, the lunar material is weakly magnetized and hysteresis effects can be neglected to first order. In this case, the linear solutions given by equations (11-4) and (11-5) can be used to determine relative permeability, because the slopes of the equations are related to permeability through equation (11-6).

Figure 11-17(a) shows a plot of radial components of the Apollo 12 LSM field (B_{Ax}) versus the geomagnetic tail field (B_{Ex}) measured by Explorer 35. A least-squares fit and slope calculations determine the factor $F = 0.0030$, which is used to determine the relative magnetic permeability for an assumed inner radius R, as shown in figure 11-4. For the bulk permeability of the Moon (the case $R = 0$),

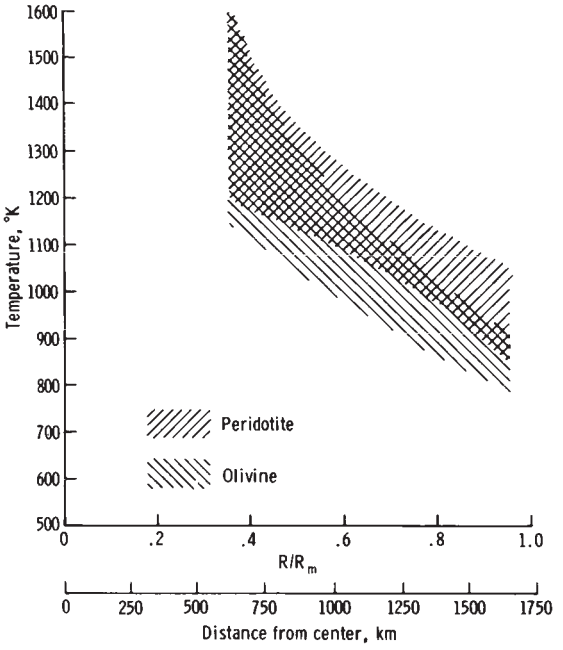

FIGURE 11-15.–Temperature estimates for assumed lunar compositions of peridotite and olivine, calculated from the electrical conductivity profile of figure 11-14.

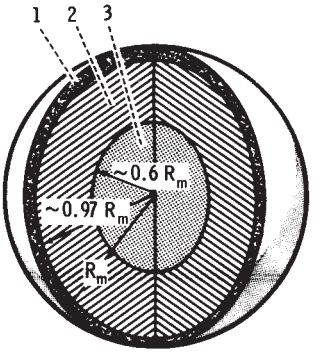

Region	Electrical conductivity, σ, mho/m	Temperature, °K	
		Olivine	Peridotite
1	$<10^{-9}$	<440	<430
2	$\sim 3.5 \times 10^{-4}$	890	1000
3	$\sim 10^{-2}$	1240	1270

FIGURE 11-16.–Conductivity and temperature contours for a three-layer Moon. Temperature calculations are based on σ as a function of temperature for pure olivine and peridotite (ref. 11-11).

μ/μ_o = 1.01 ± 0.06. For a thinner permeable shell inside the Moon, the permeability is higher, as illustrated in figure 11-17(b). A more accurate calculation of lunar permeability will be determined in the future from network measurements obtained at three locations on the lunar surface. The increased accuracy will make possible a meaningful calculation of the percentage of permeable iron in the outer layer of the lunar sphere.

Remanent Magnetic Field Interaction With the Solar Wind

Steady remanent fields have been measured at nine surface sites during the Apollo 12, 14, 15, and 16 missions. Magnitudes of these steady fields are: Apollo 12, 38 γ; Apollo 14, 103 and 43 γ at two sites separated by 1.1 km; Apollo 15, 6 γ; and Apollo 16, 121, 125, 180, 231, and 313 γ at five sites separated by distances ranging from 0.5 to 7.1 km. All these fields are attributed to remanent magnetization in nearby subsurface materials. The measurements are unexpectedly high, and their presence indicates that, at some time in the past, the Moon either possessed a strong magnetizing field or was immersed in one. A more detailed discussion of these remanent fields is available in reference 11-12 and in section 12 of this document.

Most of the measured steady fields are strong enough to interact with the solar wind plasma, provided the scale sizes of the fields are sufficiently large (ref. 11-13). The Apollo 12 site has an LSM and a solar wind spectrometer operating simultaneously, and data from both instruments have been analyzed

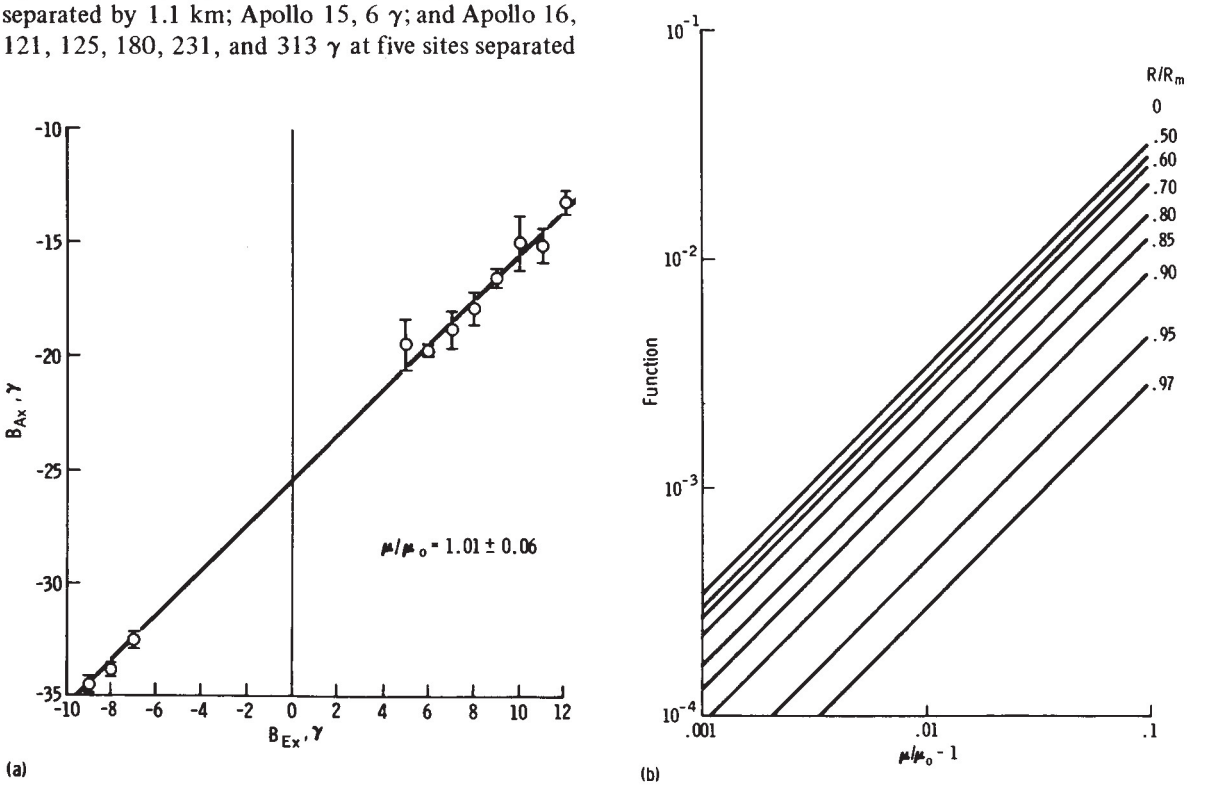

FIGURE 11-17.–Graphical representations of equations (11-4) and (11-6). (a) Radial component of Apollo 12 total surface magnetic field B_{Ax} versus the radial component of external driving field B_{Ex} (eq. (11-4)). Data points consist of measurements in quiet regions of the geomagnetic tail taken during the first four postdeployment lunations. The B_{Ax} intercept of the least-squares best-fit solid line gives the radial component of the Apollo 12 permanent field; the best-fit slope corresponds to a value of 1.01 ± 0.06 for the bulk relative permeability μ/μ_o of the Moon. (b) A graphical representation of equation (11-6), which relates the function to relative magnetic permeability $k_m = \mu/\mu_o$ for various values of R/R_m; R and R_m are internal and external radii, respectively, of a global permeable shell.

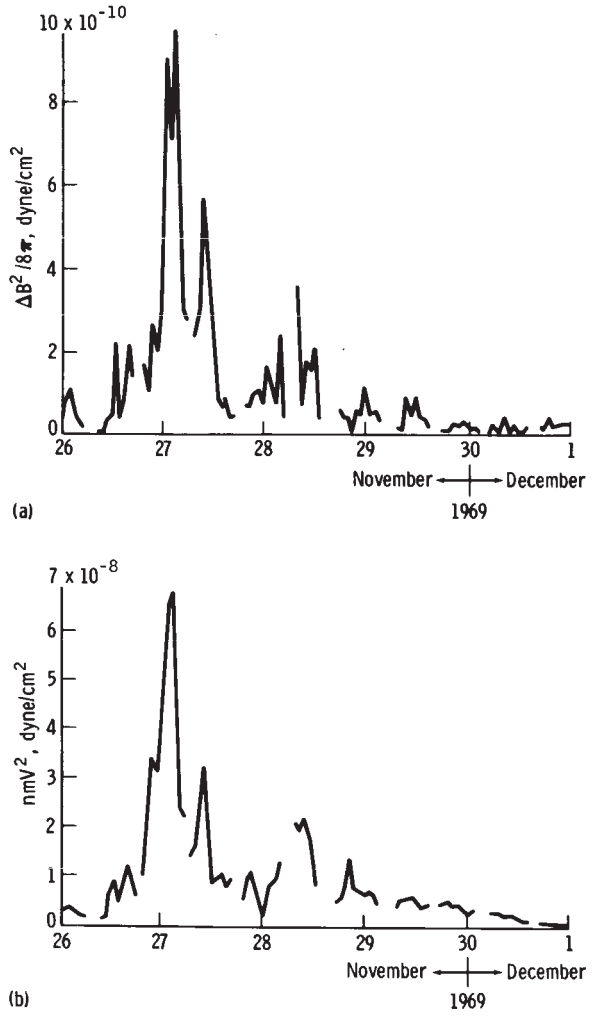

FIGURE 11-18.–Simultaneous plots of the square of (a) horizontal magnetic field difference $\Delta B^2/8\pi = 1/8\pi(\Delta B_x{}^2 + \Delta B_y{}^2 + \Delta B_z{}^2)$ where $\Delta B_i = B_{Ai} - (B_{Ei} + B_{Si})$, and i = x,y,z and (b) solar wind pressure at the Apollo 12 site, showing the correlation between the change in magnetic pressure and dynamic plasma proton pressure.

to investigate the field-plasma interaction (ref. 11-7).[1] Applying the square of equation (11-8), which allows calculation of the magnetic field difference due to the field-plasma interaction, 1-hr averages

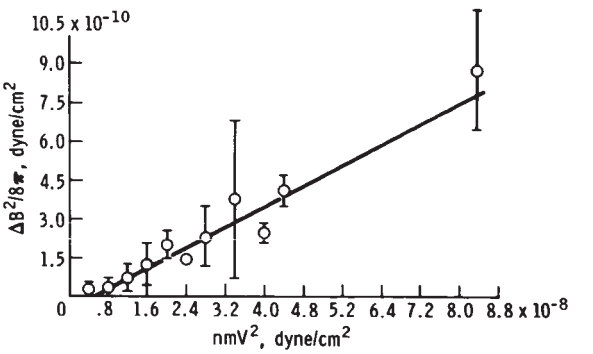

FIGURE 11-19.–Magnetic field pressure difference versus solar wind plasma dynamic pressure at the Apollo 12 site. The ratio of magnetic pressure change to plasma pressure is given by the slope to be ≈0.01. The maximum ratio of dynamic plasma pressure to total magnetic pressure $|\mathbf{B}_{ST}| = |\mathbf{B}_S + \Delta\mathbf{B}|$ is calculated to be $\beta = 5.9$.

of the magnetic pressure change $\Delta B^2/8\pi$ and simultaneous solar wind dynamic pressure nmV^2 are plotted (fig. 11-18). The correlation between the magnetic pressures is emphasized further in figure 11-19, which contains data from two sequential lunations. The correlation suggests that the field change $\Delta\mathbf{B}$ is due to a compression of the local remanent field $\mathbf{B}_S$ by the solar wind. The ratio of plasma dynamic pressure to *total* magnetic pressure is expressed

$$\beta = \frac{nmV^2}{B_{ST}^2/8\pi} \tag{11-9}$$

where $\mathbf{B}_{ST} = \mathbf{B}_S + \Delta\mathbf{B}$ is the total surface compressed field. During times of maximum plasma pressure as shown in figure 11-18, the value of β is calculated to be 5.9; $\beta \leqslant 1$ would imply that the field had been compressed to the stagnation magnitude required to stand off the solar wind and possibly form a local shock. Compression of the remanent field alone, therefore, does not cause the stagnation condition to be reached during the time period of these data. The Apollo 16 remanent magnetic fields, which exceeded 120 γ at five sites over a 7-km extent, therefore could quite possibly set up a shock during times of high solar wind pressure. Correlation of plasma data with these Apollo 16 remanent magnetic field data will be performed in future studies.

[1] Marcia Neugebauer, Conway W. Snyder, Douglas R. Clay, and B. Goldstein: Solar Wind Observations on the Lunar Surface With the Apollo 12 ALSEP. Submitted to Planetary Space Sci.

Special Events

Data for two special events are illustrated in figures 11-20 to 11-22. All magnetic field components are expressed in their respective local ALSEP surface coordinate systems ($\hat{x},\hat{y},\hat{z}$), which have origins at local deployment sites; each $\hat{x}$ is directed radially outward from the local surface; $\hat{y}$ and $\hat{z}$ are tangent to the surface and directed eastward and northward, respectively.

Apollo 15 magnetic field data for a 30-min interval during the Apollo 15 lunar module (LM) ascent on August 2, 1971, are shown in figure 11-20. The field data show evidence of plasma currents in the LM exhaust gas cloud as the gas passes the magnetometer. Some evidence of a plasma disturbance passing the magnetometer after the Apollo 15 LM impact is shown in figure 11-21. Because the LM impacted approximately 93 km away from the magnetometer, it seems surprising that the effect could travel such a large distance without attenuating

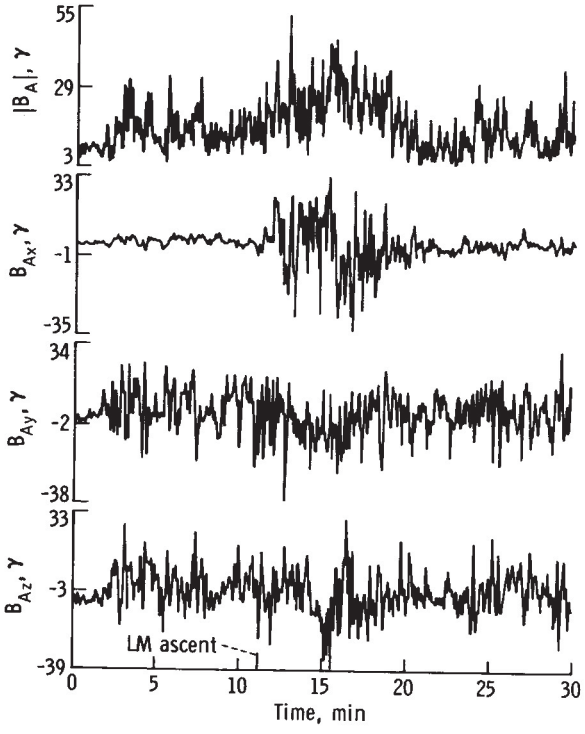

FIGURE 11-20.–Apollo 15 LSM data during lunar module ascent at 17:11 G.m.t. on August 2, 1971. The ALSEP coordinate system is used, with x directed radially outward from the surface, y eastward, and z northward. The exhaust plasma caused an increase in surface field magnitude, most evident in the x (vertical) component.

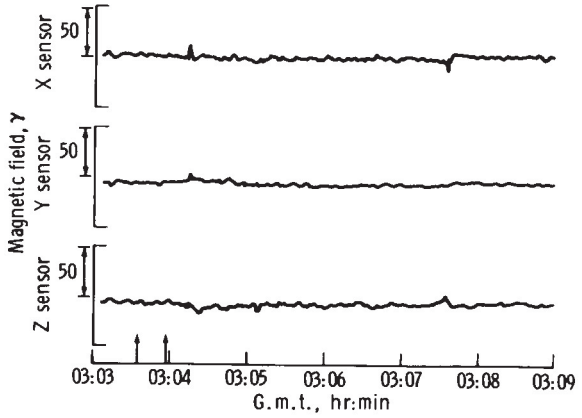

FIGURE 11-21.–Real-time data recordings of Apollo 15 LSM during the time of lunar module impact on August 3 at a position 93 km west-northwest of the magnetometer. The left arrow indicates real time of impact (03:03:35.8 G.m.t.), and the right arrow shows estimated P-wave arrival time at the Apollo 15 passive seismic experiment (ref. 11-14). The signals at 03:03:10 and 03:07:30 G.m.t. possibly show effects of the impact on the local magnetic field. Coordinate axes here refer to the respective sensor boom directions of the instrument and should not be confused with the ALSEP coordinate system used in figures 11-13, 11-17, and 11-20.

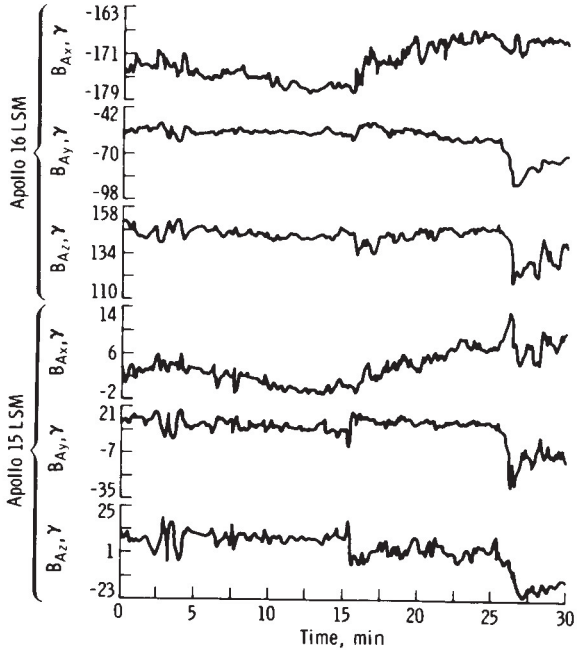

FIGURE 11-22.–Preliminary simultaneous data obtained on April 22, 1972, from Apollo 15 and Apollo 16 lunar surface magnetometers. Start time was 15:30 G.m.t. The top three vector component graphs of Apollo 16 data are shown in the Apollo 16 coordinate system; Apollo 15 components are plotted in the Apollo 15 system.

to magnitudes below instrument resolution. Both the Apollo 15 LM ascent and impact events were also observed by the Apollo 15 suprathermal ion detector experiment (ref. 11-15) and the Apollo 15 passive seismic experiment (ref. 11-14). A preliminary 30-min plot of simultaneously obtained Apollo 15 and 16 magnetometer data is shown in figure 11-22; all components are given in their respective ALSEP coordinate systems. These particular plots show that lunar induced eddy-current fields are of global rather than local extent. Future investigations using simultaneous surface magnetometer data should allow detailed analyses of lunar properties such as azimuthal variations of electrical conductivity and temperature profiles and inhomogeneities in local and global permeable material formations.

SUMMARY

Transient Magnetic Field Response, Internal Electrical Conductivity, and Temperature Implications

The electrical conductivity of the lunar interior has been determined from magnetic step transient measurements made on the lunar dark side. The general aspects of the data fit the classical theory of a conducting sphere in a magnetic field. Radial and tangential magnetic field component measurements indicate a global rather than a local response to these step transients. A continuous conductivity profile, with error limits, has been determined from normalized radial step transient response data. The conductivities, when converted to temperatures for an assumed lunar material of peridotite, suggest the existence of a thin outer layer (perhaps 90 km thick) in which the temperature rises sharply to 850° to 1050° K and then increases gradually to 1200° to 1500° K at a depth of approximately 1000 km. In the deep interior, higher temperatures are compatible with the data.

Relative Magnetic Permeability of the Moon

The whole-Moon relative permeability has been calculated to be $\mu/\mu_o = 1.01 \pm 0.06$ from measurements taken while the Moon was immersed (magnetized) in the geomagnetic tail. If an inner core of radius $R \sim 0.6\ R_m$ is above the Curie temperature (1073° K), the permeability of the outer shell will still lie within the limits listed above.

Remanent Magnetic Field Interaction With the Solar Wind

The remanent magnetic fields measured thus far on the Moon are 38 γ at Apollo 12 in Oceanus Procellarum, 103 and 43 γ at two Apollo 14 Fra Mauro sites separated by 1.1 km, 6 γ at the Apollo 15 Hadley-Apennine site, and 121 to 313 γ at the Apollo 16 Descartes highland site.

Measurements show that the remanent field at the Apollo 12 site is compressed by the solar wind. The 38 γ remanent field is compressed to 54 γ by a solar wind pressure increase of 7×10^{-8} dyne/cm^2. The ratio of plasma dynamic pressure to total magnetic pressure β is 5.9 during the time of maximum field compression. The change in magnetic pressure is directly proportional to the change in plasma dynamic pressure.

REFERENCES

11-1. Dyal, Palmer; and Parkin, Curtis W.: The Apollo 12 Magnetometer Experiment: Internal Lunar Properties From Transient and Steady Magnetic Field Measurements. Proceedings of the Second Lunar Science Conference, vol. 3, A. A. Levinson, ed., MIT Press (Cambridge, Mass.), 1971, pp. 2391-2413.

11-2. Dyal, Palmer; and Parkin, Curtis W.: Electrical Conductivity and Temperature of the Lunar Interior From Magnetic Transient-Response Measurements. J. Geophys. Res., vol. 76, no. 25, Sept. 1, 1971, pp. 5947-5969.

11-3. Smythe, W. R.: Static and Dynamic Electricity. McGraw-Hill Book Co. (New York), 1950.

11-4. Snyder, Conway W.; Clay, Douglas R.; and Neugebauer, Marcia: The Solar-Wind Spectrometer Experiment. Sec. 5 of Apollo 12 Preliminary Science Report. NASA SP-235, 1970.

11-5. Dyal, Palmer; Parkin, Curtis W.; and Cassen, Patrick: Surface Magnetometer Experiments: Internal Lunar Properties and Lunar Field Interactions With the Solar Plasma. Proceedings of the Third Lunar Science Conference, vol. 3, David R. Criswell, ed., MIT Press (Cambridge, Mass.), 1972, pp. 2287-2308.

11-6. Dyal, Palmer; and Parkin, Curtis W.: Lunar Properties From Transient and Steady Magnetic Field Measurements. The Moon, vol. 4, nos. 1 and 2, Apr. 1972, pp. 63-87.

11-7. Dyal, P.; Parkin, C. W.; Snyder, C. W.; and Clay, D. R.: Measurements of Lunar Magnetic Field Interaction With the Solar Wind. Nature, vol. 236, no. 5347, Apr. 21, 1972, pp. 381-385.

11-8. Dyal, Palmer; Parkin, Curtis W.; and Sonett, C. P.: Lunar Surface Magnetometer. IEEE Trans. Geosci. Electron., vol. GE-8, no. 4, Oct. 1970, pp. 203-215.

11-9. Gordon, D. I.; Lundsten, R. H.; and Chiarodo, R. A.: Factors Affecting the Sensitivity of Gamma-Level Ring-Core Magnetometers. IEEE Trans. Magnetics, vol. MAG-1, no. 4, Dec. 1965, pp. 330-337.

11-10. Gordon, Daniel I.; and Brown, Robert E.: Recent Advances in Fluxgate Magnetometers. IEEE Trans. Magnetics, vol. MAG-8, no. 1, Mar. 1972, pp. 76-82.

11-11. England, A. W.; Simmons, G.; and Strangway, D.: Electrical Conductivity of the Moon. J. Geophys. Res., vol. 73, no. 10, May 15, 1968, pp. 3219-3226.

11-12. Dyal, P.; Parkin, C. W.; Sonett, C. P.; DuBois, R. L.; and Simmons, G.: Lunar Portable Magnetometer Experiment. Sec. 13 of Apollo 14 Preliminary Science Report. NASA SP-272, 1971.

11-13. Barnes, A.; Cassen, P.; Mihalov, J. D.; and Eviatar, A.: Permanent Lunar Surface Magnetism and Its Deflection of the Solar Wind. Science, vol. 172, no. 3984, May 14, 1971, pp. 716-718.

11-14. Latham, G. V.; Ewing, M.; Press, F.; Sutton, G.; et al.: Passive Seismic Experiment. Sec. 8 of Apollo 15 Preliminary Science Report. NASA SP-289, 1972.

11-15. Hills, H. K.; Meister, J. C.; Vondrak, R. R.; and Freman, J. W., Jr.: Suprathermal Ion Detector Experiment (Lunar Ionosphere Detector). Sec. 12 of Apollo 15 Preliminary Science Report. NASA SP-289, 1972.

ACKNOWLEDGMENTS

The authors express their appreciation for the efforts of the many persons who contributed to this experiment. In particular, thanks are extended to John Keeler, Fred Bates, Kenneth Lewis, and Marion Legg, whose diligent efforts contributed to the success of this experiment. The authors also wish to thank Dr. C. W. Snyder and Dr. D. R. Clay, Jet Propulsion Laboratory, for the use of Apollo 12 solar wind spectrometer data.